Research Square

Preprints are preliminary reports that have not undergone peer review.
They should not be considered conclusive, used to inform clinical practice,
or referenced by the media as validated information.

Comparative RNA-seq analysis reveals shared and distinct molecular features of natural ovarian aging versus chemotherapy-induced premature ovarian insufficiency

Yuanmeng Zhang
The Second Hospital of Hebei Medical University
Ni Yang
The Second Hospital of Hebei Medical University
Shangxuan Song
Hebei Medical University
Chunli Qin
The Second Hospital of Hebei Medical University
Yuanzheng Ning
Hebei International Studies University
Yingqian Wang
The Second Hospital of Hebei Medical University
Yanyan Liu
The Second Hospital of Hebei Medical University
Xiaotong Xu
The Second Affiliated Hospital of Xi'an Jiaotong University
Jiahua Zheng
The Second Hospital of Hebei Medical University
Jingkun Zhang
The Second Hospital of Hebei Medical University
Zhongkang Li
zhongkangli@hebmu.edu.cn
The Second Hospital of Hebei Medical University
Xianghua Huang
The Second Hospital of Hebei Medical University

Research Article

Keywords: Aging, Apoptosis, Fibrosis, Primary Ovarian Insufficiency, Transcriptome

Posted Date: November 20th, 2026

DOI: https://doi.org/10.21203/rs.3.rs-11562501/v1

License: This work is licensed under a Creative Commons Attribution 4.0 International License.
Read Full License

Additional Declarations: No competing interests reported.

Abstract

Purpose

To determine whether chemotherapy-induced premature ovarian insufficiency (POI) reproduces the functional, histological, and molecular features of natural ovarian aging in mice.

Methods

Twelve-month-old female C57BL/6 mice served as the natural aging group; eight-week-old mice received cyclophosphamide (120 mg/kg) and busulfan (30 mg/kg) to induce POI. Young mice were controls. Ovarian reserve, estrous cyclicity, serum hormones, fertility, tissue injury, and whole-ovary transcriptomes were compared.

Results

Both models showed follicular depletion, irregular estrous cycles, altered reproductive hormones, reduced fertility, oxidative stress, and apoptosis. Natural aging was associated with greater p16/p21 staining, collagen deposition, and stromal fibrosis. Chemotherapy-induced POI displayed stronger γH2AX staining, oxidative injury, and apoptosis. Transcriptomic profiling revealed shared changes in PI3K/Akt, AMPK, and FoxO-associated signaling, alongside model-related differences in immune, inflammatory, and metabolic enrichment patterns. Selected gene-expression patterns were supported by quantitative PCR.

Conclusions

Chemotherapy-induced POI reproduces important manifestations of natural ovarian aging but differs in its predominant injury profile. These differences should guide the selection and interpretation of ovarian dysfunction models.

Introduction

The ovary is one of the earliest organs in the female reproductive and endocrine systems to exhibit age-related functional decline. Ovarian aging refers to the gradual deterioration and eventual exhaustion of ovarian function and can broadly be classified into physiological and pathological aging. With advancing age, the ovarian follicular reserve progressively declines, oocyte quality deteriorates, and abnormalities in sex hormone secretion, estrous or menstrual cyclicity, and fertility gradually emerge. This naturally occurring age-related process is generally referred to as physiological ovarian aging [1, 2]. In contrast, premature ovarian insufficiency (POI) refers to impaired ovarian function occurring before the age of 40 years. Its etiology is highly heterogeneous and includes genetic, immune, and iatrogenic factors, among

which chemotherapy-induced ovarian injury has been extensively investigated [3, 4]. Although natural aging and POI differ substantially in their timing of onset and initiating factors, both can ultimately lead to reduced follicular reserve, endocrine dysfunction, and impaired fertility and therefore share several phenotypic similarities [5, 6]. With the increasing postponement of childbearing and improved long-term survival among patients with cancer, accurately understanding ovarian functional decline caused by different etiologies and selecting appropriate experimental models and intervention strategies have become important issues in reproductive aging and fertility preservation research.

Animal models are essential for investigating ovarian functional decline and evaluating potential therapeutic approaches. Naturally aged mice reproduce the progressive ovarian changes that occur with advancing age, although these models require a relatively long experimental period and are inevitably influenced by age-related systemic changes. In contrast, chemically induced models can be established rapidly and generally produce reproducible ovarian injury, which has led to their widespread use in studies of POI and ovarian dysfunction. Natural aging models have also been used to evaluate treatments aimed at restoring ovarian function. For example, Lin et al. [7] reported in Science in 2026 that finerenone improved follicular development and ovarian fibrosis in aged mice and subsequently extended these findings to patients with POI. This raises an important question. If natural aging and POI models are used interchangeably because they produce similar ovarian phenotypes, important differences in their underlying pathology may be overlooked. Such differences could affect both the interpretation of experimental findings and the expected range of therapeutic effects. Cyclophosphamide (CTX), cisplatin, and busulfan (Bus) are among the chemotherapeutic agents commonly used to establish POI models [8–10]. Combined treatment with CTX and Bus causes sustained follicular depletion and impaired ovarian endocrine function and is therefore widely used to induce POI in mice [11, 12].

Natural ovarian aging and POI share a similar final outcome, namely a decline in ovarian reserve. However, a similar outcome does not necessarily mean that the two conditions arise from the same biological processes. Many studies evaluating stem cells, extracellular vesicles, and pharmacological treatments for POI use chemotherapy-induced models to assess therapeutic efficacy. The rapid ovarian injury caused by chemotherapy, however, may differ considerably from the gradual tissue and molecular changes that accumulate during natural aging. A treatment that improves ovarian function after chemotherapy-induced injury may therefore not have the same effect on an aging ovary. Identifying which changes are shared by the two models and which are specific to each one may help clarify the common biology of ovarian functional decline. It may also allow treatment effects observed in different animal models to be interpreted more accurately.

In this study, we directly compared natural reproductive aging with chemically induced POI in mice. Twelve-month-old C57BL/6 female mice were used as the natural reproductive aging model, while young adult mice were treated with CTX and Bus and evaluated 28 days later to establish the POI model. Young adult mice served as normal controls. We compared estrous cyclicity, follicular reserve, ovarian index, endocrine function, and fertility across the three groups. We also examined apoptosis, oxidative stress,

cellular senescence, and fibrosis to characterize differences in ovarian tissue injury. Ovarian transcriptomes were then analyzed to identify molecular changes shared by the two models and changes that differed between them. Representative differentially expressed genes were further examined to assess whether their expression patterns were consistent with the transcriptomic results. By combining functional, histological, and transcriptomic findings, we aimed to clarify the similarities and differences between natural reproductive aging and chemically induced POI. The results may also help define when chemotherapy-induced POI is an appropriate experimental model for ovarian aging and when differences between the two conditions need to be considered.

Materials and methods

Animals

Female C57BL/6 mice were obtained from the Laboratory Animal Center of Hebei Medical University, China, and used to establish models of natural ovarian aging and chemotherapy-induced premature ovarian insufficiency. All mice were housed under specific pathogen-free conditions in a temperature- and humidity-controlled environment with a 12-h light/dark cycle and ad libitum access to food and water. All animal experiments were conducted in accordance with institutional guidelines for the care and use of laboratory animals and were approved by the Animal Ethics Committee of the Second Hospital of Hebei Medical University (approval no. 2026-AE407).

The animals were divided into three groups: a young control (CON) group, a natural aging (NA) group, and a chemotherapy-induced premature ovarian insufficiency (POI) group. Twelve-month-old female C57BL/6 mice were assigned to the NA group, whereas eight-week-old female C57BL/6 mice were used for the CON and POI groups. POI was induced by a single intraperitoneal injection of cyclophosphamide at 120 mg/kg and busulfan at 30 mg/kg. Animals were followed for 28 days after treatment. Body weight was recorded throughout the experimental period. At the end of the study, blood samples and both ovaries were collected for histological, biochemical, hormonal, and molecular analyses (Fig. 1). At the experimental endpoint, mice were anesthetized with inhaled isoflurane and subsequently euthanized by an overdose of isoflurane (5%). Death was confirmed by the cessation of respiration and heartbeat. All procedures were performed in accordance with the institutionally approved animal experimental protocol.

Serum hormone measurements

Blood samples were collected from the orbital venous plexus of mice during diestrus. Serum was separated by centrifugation at 4,000 × g for 10 min at 4°C and stored at − 80°C until analysis. Serum estradiol (E2), follicle-stimulating hormone (FSH), and luteinizing hormone (LH) concentrations were measured using commercially available ELISA kits (Cloud-Clone, China) according to the manufacturer's

instructions. Absorbance was measured at 450 nm using a microplate reader, and hormone concentrations were calculated based on the corresponding standard curves.

Estrous cycle monitoring

Estrous cycles were monitored by vaginal cytology. Vaginal exfoliated cells were collected at the same time each day, prepared as smears, and stained with hematoxylin and eosin. Smears were examined under a light microscope. Based on the relative proportions of nucleated epithelial cells, cornified epithelial cells, and leukocytes, each sample was classified as proestrus (P), estrus (E), metestrus (M), or diestrus (D). Cycle patterns were recorded for each mouse, and the frequencies of normal, prolonged, and irregular cycles were compared among the three groups.

Ovarian index, histological examination, and follicle counting

At the end of the experiment, both ovaries were collected and surrounding adipose and connective tissues were carefully removed. Ovarian weight was recorded, and the ovarian index was calculated relative to body weight. Ovarian tissues were fixed in 4% paraformaldehyde, dehydrated through graded ethanol, embedded in paraffin, and serially sectioned.

After deparaffinization and rehydration, sections were stained with hematoxylin and eosin. Ovarian morphology and follicles at different developmental stages were examined under a light microscope. Primordial, primary, secondary, antral, and atretic follicles were classified according to their morphological characteristics and counted for comparisons among groups.

TUNEL staining

Apoptosis in ovarian tissue was evaluated using TUNEL staining. Paraffin-embedded ovarian sections were deparaffinized and rehydrated, followed by staining with a TUNEL apoptosis detection kit (Servicebio, China) according to the manufacturer's instructions. Sections were incubated at 37°C in the dark and counterstained with DAPI (Servicebio, China). After mounting with antifade medium, fluorescence images were acquired under identical imaging conditions.

Images were analyzed using ImageJ. The proportion of TUNEL-positive cells was calculated to evaluate apoptosis in ovarian tissue.

Senescence-associated β-galactosidase staining

Senescence-associated β-galactosidase staining was used to assess cellular senescence in ovarian tissue. Frozen ovarian sections were prepared and stained using an SA-β-gal staining kit (Servicebio, China) according to the manufacturer's instructions. Positive blue-green staining was examined under a

microscope. ImageJ was used to calculate the SA-β-gal-positive area relative to the total ovarian tissue area.

Western blot analysis

Western blot analysis
Ovarian tissues were lysed in RIPA buffer (Servicebio, China) containing protease and phosphatase inhibitor mixtures (Servicebio, China). Protein concentrations were determined using a BCA Protein Assay Kit (Thermo Fisher Scientific, USA). Equal amounts of denatured protein were separated by 10% or 12.5% SDS-PAGE (Biotides, China) and transferred onto PVDF membranes (Millipore, USA).

After blocking with 5% skim milk (Solarbio, China) for 1 h at room temperature, membranes were incubated overnight at 4°C with primary antibodies against Bcl-2 (1:1000, Zen Bioscience, China), Caspase-3 (1:1000, Zen Bioscience, China), Caspase-9 (1:1000, Zen Bioscience, China), and β-actin (1:4000, Servicebio, China). Membranes were then incubated with the appropriate HRP-conjugated secondary antibodies, including anti-mouse IgG-HRP at 1:10,000 and anti-rabbit IgG-HRP at 1:15,000 (Mei5bio, China), for 1 h at room temperature. Protein signals were detected using a ChemiDoc MP Imaging System (Bio-Rad, USA), and band intensities were quantified using ImageJ.

Immunohistochemistry

Immunohistochemistry was performed to evaluate proteins associated with cellular senescence, DNA damage, and extracellular matrix remodeling. Paraffin-embedded ovarian sections were deparaffinized, rehydrated, and subjected to antigen retrieval. Endogenous peroxidase activity and nonspecific binding were blocked before overnight incubation at 4°C with primary antibodies against p16 (1:1000, Zen Bioscience, China), p21 (1:1000, Zen Bioscience, China), γH2AX (1:1000, Zen Bioscience, China), and Collagen I (1:1000, Zen Bioscience, China).

Sections were subsequently incubated with the corresponding secondary antibodies (Servicebio, China), developed using DAB (Servicebio, China), and counterstained with hematoxylin (Servicebio, China). Images were acquired using identical microscope settings across groups. Positive staining was quantified using ImageJ and expressed as positive area or as the proportion of positive area relative to total ovarian tissue area.

Assessment of Ovarian Oxidative Stress

Oxidative stress in ovarian tissue was assessed by measuring reactive oxygen species (ROS), malondialdehyde (MDA, Servicebio, China), glutathione peroxidase (GSH-Px, Servicebio, China), and total superoxide dismutase (T-SOD, Servicebio, China).

ROS levels were measured using the fluorescent probe dihydroethidium (DHE, Servicebio, China). Fresh ovarian tissues were homogenized in homogenization buffer and centrifuged at 10,000 × g for 10 min at 4°C. The supernatant was transferred to a black 96-well plate and incubated with DHE working solution at 37°C for 20 min in the dark. Fluorescence was measured using a microplate reader with excitation at 520 nm and emission at 605 nm. ROS levels were expressed as relative fluorescence units normalized to protein content. MDA levels and GSH-Px and T-SOD activities were measured using the corresponding commercial kits according to the manufacturers' instructions.

Masson and Sirius Red Staining

Masson trichrome and Sirius Red staining were used to evaluate collagen deposition and ovarian fibrosis. Paraffin sections were deparaffinized and rehydrated before staining with Masson trichrome or Sirius Red reagents (Servicebio, China) according to the manufacturer's instructions.

Collagen distribution within the ovarian stroma and around follicles was examined under a light microscope. Images were acquired under identical conditions and analyzed using ImageJ. Fibrosis was quantified as the collagen-positive area relative to the total ovarian tissue area.

Fertility Assessment

To evaluate reproductive capacity, females from each experimental group were housed with adult male mice of confirmed fertility. Pregnancy and delivery were monitored, and both successful delivery and the number of live-born offspring were recorded for each female. Fertility was evaluated using the number of live-born pups per female and the proportion of females that successfully delivered.

RNA Extraction and Transcriptome Sequencing

Frozen ovarian tissues were ground thoroughly in liquid nitrogen, and total RNA was extracted using TRIzol Reagent (Thermo Fisher Scientific, USA) according to the manufacturer's instructions. Chloroform was added for phase separation, followed by centrifugation at 4°C. The aqueous phase was collected, and RNA was precipitated with isopropanol. The RNA pellets were washed with 75% ethanol and dissolved in RNase-free water.

RNA concentration was measured using a Qubit 3.0 Fluorometer (Thermo Fisher Scientific, USA). RNA integrity was evaluated using a Qsep100 nucleic acid analyzer (Bioptic, Taiwan, China) and agarose gel electrophoresis. Three biological replicates from each group that met the quality requirements were used for library preparation and sequencing.

RNA library preparation and high-throughput sequencing were performed by Shanghai Hao Wei Tai Biotechnology Co., Ltd. (Shanghai, China). Sequencing libraries were generated from qualified RNA samples and sequenced on an Illumina NovaSeq 6000 platform using a 150-bp paired-end sequencing strategy. Raw sequencing reads were subjected to quality control and adapter trimming to obtain high-quality clean reads. Clean reads were aligned to the mouse reference genome GRCm39 using HISAT2. Gene-level read counts were generated using featureCounts.

Differential gene expression analysis was performed using DESeq2. Genes with an absolute log2 fold change of at least 1 and an adjusted P value below 0.05 were considered differentially expressed. Gene Ontology (GO) and Kyoto Encyclopedia of Genes and Genomes (KEGG) pathway enrichment analyses were performed using the R package clusterProfiler. Gene set enrichment analysis (GSEA) was performed using genes ranked according to their differential expression statistics. Pathways with an adjusted P value below 0.05 were considered significantly enriched.

qRT-PCR Validation

Quantitative real-time PCR was performed to validate the expression of representative genes identified from the transcriptomic analysis. Total RNA was extracted from ovarian tissues using TriQuick Reagent (Solarbio, Beijing, China). One microgram of total RNA was reverse-transcribed into cDNA using the SureScript First-Strand cDNA Synthesis Kit (GeneCopoeia, USA) according to the manufacturer's instructions.

Real-time PCR was performed using NovoStart Universal Fast SYBR qPCR SuperMix (Novoprotein, Suzhou, China) on an FQD-96A real-time PCR system (Bioer Technology Co., Hangzhou, China). The amplification program consisted of initial denaturation at 95°C for 3 min, followed by 40 cycles of denaturation at 95°C for 15 s and annealing and extension at 60°C for 30 s. Gapdh was used as the internal reference gene. Relative mRNA expression was calculated using the 2^−ΔΔCt method. Primer sequences are provided in Supplementary Table S1.

Statistical Analysis

Statistical analyses were performed using Origin 2024. Data are presented as mean ± SD unless otherwise indicated. Normality and homogeneity of variance were assessed before group comparisons. Comparisons among three groups were performed using one-way analysis of variance followed by Tukey's multiple-comparison test when the assumptions of normality and homogeneity of variance were satisfied. When these assumptions were not met, the Kruskal-Wallis test followed by an appropriate post hoc multiple-comparison test was used.

Changes in body weight over time were analyzed using two-way repeated-measures analysis of variance, with treatment group and time included as factors, followed by multiple-comparison testing when appropriate. Categorical variables, including delivery outcomes and estrous cycle classifications, were analyzed using the χ^2 test or Fisher's exact test as appropriate. All tests were two-sided, and $P < 0.05$ was considered statistically significant.

Results

Natural aging and chemotherapy-induced POI share ovarian functional and reproductive endocrine impairment

Vaginal cytology showed the characteristic cell populations of the four stages of the mouse estrous cycle (Fig. 1A). Young control mice maintained relatively regular cycles, whereas both naturally aged mice and mice with chemotherapy-induced POI showed prolonged or irregular cycles to varying degrees (Fig. 1B). Cycle patterns were assessed in eight mice per group. All mice in the CON group maintained normal estrous cycles. Irregular cycles predominated in the NA group, with several mice also showing prolonged cycles. Clear cycle abnormalities were also observed in the POI group, although a small proportion of mice retained a normal cycle pattern (Fig. 1F).

Body weight followed different trajectories among the three groups. Control mice gradually gained weight during the observation period, whereas naturally aged mice remained heavier overall with mild fluctuations. In contrast, body weight progressively decreased after chemotherapy treatment in the POI group (Fig. 1G).

Histological examination showed preserved ovarian architecture in young control mice, with follicles at multiple developmental stages. Both NA and POI ovaries contained fewer healthy follicles and more atretic follicles (Fig. 1C, D). The ovarian index was lower in both groups than in controls (both $P < 0.0001$), with the lowest values observed in the POI group (Fig. 1E).

Serum E2 levels were reduced in both NA and POI mice compared with controls (both $P < 0.01$), with no significant difference between the two experimental groups (Fig. 1H). FSH and LH levels were also increased in both NA and POI mice compared with CON. Both hormones differed significantly between NA and CON (both $P < 0.001$) and between POI and CON (both $P < 0.01$), whereas no significant difference was detected between NA and POI (Fig. 1I, J).

Chemotherapy-induced POI exhibits more pronounced ovarian apoptosis than natural aging

TUNEL staining showed an increase in apoptotic cells in both experimental groups, with the strongest signal detected in POI ovaries (Fig. 2A, C). Naturally aged ovaries also showed more TUNEL-positive cells than controls, although the increase was less marked.

SA-β-gal staining revealed larger positive areas in both NA and POI ovaries compared with young controls (Fig. 2B, D). The extent of SA-β-gal staining was similar between the two experimental groups, indicating that senescence-associated changes were present in both conditions.

We next examined apoptosis-related proteins by Western blotting. Caspase-3 and Caspase-9 were increased in both NA and POI ovaries, whereas Bcl-2 was reduced compared with controls (Fig. 2E, F). The changes were generally stronger in the POI group, consistent with the more extensive TUNEL staining.

Natural aging and chemotherapy-induced POI display different patterns of ovarian senescence and oxidative

damage

Immunohistochemical analysis showed increased staining for p21, p16, γH2AX, and Collagen I in both NA and POI ovaries compared with controls (Fig. 3A to E). The patterns differed among markers. p21 and p16 staining was more prominent in naturally aged ovaries, while γH2AX showed its strongest increase in the POI group (Fig. 3B to D).

Collagen I staining was limited in control ovaries but increased in both experimental groups. The largest positive area was observed in the NA group, whereas the increase in POI ovaries was more moderate (Fig. 3A, E).

Oxidative stress measurements showed increased MDA and ROS levels in both NA and POI ovaries compared with controls (Fig. 3F, G). The highest values were generally observed in the POI group. GSH-Px activity was reduced in both experimental groups, with little difference between NA and POI (Fig. 3H). T-SOD activity decreased progressively across CON, NA, and POI, with the greatest reduction after chemotherapy treatment (Fig. 3I).

The stronger γH2AX accumulation and oxidative stress in POI contrasted with the higher p16, p21, and Collagen I signals detected in naturally aged ovaries.

Natural aging is associated with greater ovarian fibrosis and reduced fertility

Masson trichrome and Sirius Red staining showed increased collagen deposition in both NA and POI ovaries compared with controls (Fig. 4A, B). Fibrotic areas were more extensive in naturally aged ovaries and were particularly evident in the ovarian stroma and around follicles. POI ovaries also showed increased collagen deposition, but the overall extent was lower than in the NA group. Representative gross images of ovaries from the three groups are shown in Fig. 4D.

Quantification of Masson and Sirius Red staining confirmed the histological observations, with the highest collagen-positive area detected in naturally aged ovaries (Fig. 4E).

Representative photographs of reproductive outcomes following mating are presented in Fig. 4C. Reproductive performance was markedly reduced in both experimental groups. The number of live-born pups per female was lower in NA and POI mice than in controls, while no significant difference was detected between the two experimental groups (Fig. 4F).

All eight females in the CON group delivered successfully. In comparison, successful delivery occurred in one of eight NA females and four of eight POI females (Fig. 4G). Although the difference between NA and POI did not reach a clear statistical distinction, naturally aged mice showed a poorer delivery outcome in this cohort.

Transcriptomic profiling reveals shared and distinct molecular features of natural aging and chemotherapy-induced POI

Transcriptome sequencing was performed on ovarian tissues from the three groups. Hierarchical clustering showed clear differences in gene expression profiles among CON, NA, and POI samples (Fig. 5A).

Differential expression analysis identified 345 upregulated and 732 downregulated genes in NA ovaries compared with CON. In POI ovaries, 568 genes were upregulated and 711 were downregulated relative to controls (Fig. 5B, C). Comparison of the two DEG sets showed both overlapping and model-associated transcriptional changes (Fig. 5D).

KEGG enrichment analysis identified several pathways altered in both models, including PI3K/Akt signaling, hormone-related pathways, AMPK signaling, and FoxO signaling (Fig. 5E). GSEA showed similar enrichment patterns for several representative pathways in NA and POI ovaries relative to controls (Fig. 5F, G).

Gene Ontology Biological Process enrichment analysis further revealed differences in the functional categories associated with the two models. In naturally aged ovaries, differentially expressed genes were enriched for processes related to leukocyte adhesion, migration, activation, and immune cell regulation (Fig. 5H). In chemotherapy-induced POI ovaries, enriched processes included inflammatory responses, regulation of the ERK1/ERK2 cascade, and lipid and fatty acid metabolism (Fig. 5I).

These findings suggest that natural aging and chemotherapy-induced POI involve partially overlapping but distinct transcriptional responses. The enrichment results should be interpreted as associations with biological processes rather than direct evidence of pathway activation.

Validation of representative differentially expressed genes

Representative genes were selected from the pathways identified by transcriptomic analysis and examined by qRT-PCR (Fig. 6). In naturally aged ovaries, the Wnt signaling-related genes *Fzd10* and *Wnt4* were reduced, whereas *Itga7* and *Col1a1*, which are associated with extracellular matrix regulation, were increased.

A different expression pattern was observed in chemotherapy-induced POI. The stress- and apoptosis-related genes *Ddit3* and *Fasl* were increased, while the inflammatory genes *Tnf* and *Il1b* also showed higher expression.

FoxO signaling was altered in both models in the transcriptomic analysis. The representative genes *Irs4* and *Sgk1* did not differ significantly between NA and POI, although both experimental groups differed

from CON. The qRT-PCR results were therefore broadly consistent with the pathway patterns identified by RNA sequencing.

Discussion

Oxidative stress has long been implicated in the decline of ovarian function. Follicular development, ovulation, and corpus luteum formation all depend on active mitochondrial metabolism and tightly regulated redox homeostasis. When reactive oxygen species exceed the capacity of endogenous antioxidant systems, mitochondrial dysfunction, lipid peroxidation, protein damage, and DNA damage can follow, with direct consequences for granulosa cell survival and oocyte quality [13–15]. Redox balance also becomes progressively disturbed with reproductive aging and has been linked to declining oocyte competence, cellular senescence, and changes in the ovarian microenvironment [16].

In our study, both naturally aged and chemotherapy-induced POI ovaries showed increased ROS and MDA, accompanied by reduced GSH-Px and T-SOD activity. Oxidative stress was therefore evident in both forms of ovarian dysfunction rather than being restricted to chemotherapy-related injury. FoxO signaling was also altered in both groups at the transcriptomic level. The POI group, however, showed stronger ROS accumulation, higher MDA levels, a greater reduction in T-SOD activity, and more pronounced γH2AX staining. This pattern is consistent with the known effects of cyclophosphamide and busulfan, which can rapidly induce DNA damage, mitochondrial stress, and disruption of cellular redox balance.

Natural aging showed a somewhat different profile. Oxidative damage was present, but p16, p21, and Collagen I were more strongly increased than in chemotherapy-induced POI. A single measurement of ROS may not fully reflect the cumulative effects of oxidative stress during aging. Persistent redox imbalance and progressive mitochondrial dysfunction may act over time together with DNA damage responses and cellular senescence to reshape the ovarian stromal environment. Collagen deposition and increased tissue stiffness have been reported as prominent features of the aging ovary [17]. Our results are consistent with this view, although the present experimental design does not directly resolve how these changes develop over time.

Apoptosis is another major contributor to follicular atresia and loss of ovarian reserve [18, 19]. TUNEL-positive cells increased in both NA and POI ovaries, accompanied by increased Caspase-3 and Caspase-9 expression and reduced Bcl-2. The magnitude of these changes was greater after chemotherapy. The transcriptomic data showed a similar pattern, with apoptosis-related signaling more prominent in the POI group and increased expression of stress- and apoptosis-related genes such as *Ddit3* and *Fasl*.

Inflammatory signaling was also more apparent in chemotherapy-induced POI. JAK/STAT and NF-κB-related pathways were enriched, while *Tnf* and *Il1b* showed increasing expression. These changes occurred alongside increased ROS, γH2AX, TUNEL staining, Caspase-3, and Caspase-9. Rather than representing isolated abnormalities, these signals may reflect different components of the same injury response triggered by chemotherapy. Natural aging also involved apoptosis, but the changes were less pronounced than those observed in POI.

The difference between the two models was particularly clear at the level of extracellular matrix remodeling. Masson staining, Sirius Red staining, and Collagen I immunohistochemistry all showed greater collagen deposition in naturally aged ovaries, particularly in the ovarian stroma and around follicles [20]. Collagen also increased in POI ovaries, but the extent of fibrosis was lower than in the NA group.

The transcriptomic findings were consistent with the histological observations. ECM-receptor interaction, Wnt signaling, and pathways related to tissue homeostasis and remodeling were more prominent in naturally aged ovaries. *Col1a1* and *Itga7* showed corresponding changes on further validation. These results fit well with previous studies showing that stromal fibrosis increases with reproductive age. Briley et al. [21] reported progressive accumulation of ovarian stromal collagen with aging, accompanied by increased Sirius Red staining and hydroxyproline content.

Age-related changes in the ovary are not limited to collagen abundance. The composition and mechanical properties of the extracellular matrix also change with age, and older ovaries become measurably stiffer. Follicles develop within this surrounding tissue environment and depend on interactions among granulosa cells, theca cells, vascular cells, immune cells, and the extracellular matrix [22–24]. Increased matrix stiffness can alter cell-matrix signaling and the physical environment required for follicular growth. Experimental models that reproduce the stiffness of the aging ovarian matrix have also been shown to impair follicular development and oocyte quality. This provides a plausible link between the stronger fibrotic phenotype observed in the NA group and the marked decline in reproductive function.

Fertility provides a functional endpoint that cannot be captured by histological or molecular markers alone. In the present study, both NA and POI mice produced fewer offspring than young controls. The reproductive outcome of naturally aged mice was not better than that of the POI group, despite the stronger oxidative injury, DNA damage, and apoptosis observed after chemotherapy.

All eight control females delivered successfully, whereas successful delivery occurred in only one of eight naturally aged females and four of eight POI females. The limited sample size does not allow a firm conclusion regarding the difference between NA and POI, but the pattern is notable. The severity of individual damage markers did not closely parallel the final reproductive outcome.

This difference may reflect the broader range of factors that determine fertility in an aging animal. Successful reproduction depends not only on the number of remaining follicles but also on oocyte quality. With increasing reproductive age, oocytes accumulate mitochondrial abnormalities, redox imbalance, spindle defects, and chromosome segregation errors. Granulosa cells, follicular fluid, and the surrounding stromal environment also undergo age-dependent changes. The aging ovarian microenvironment has been associated with inflammation, fibrosis, increased tissue stiffness, and oxidative damage [25], all of which may influence the developmental competence of the remaining oocytes.

These observations are also relevant when ovarian models are used to evaluate potential treatments. Changes in E2, FSH, follicle number, apoptosis, or oxidative stress provide useful measures of ovarian injury, but they do not necessarily predict restoration of reproductive capacity. Ovulation, oocyte quality, pregnancy, and live birth remain important functional outcomes when assessing whether an intervention has meaningfully improved ovarian function. The present comparison also shows that natural reproductive aging and chemotherapy-induced POI can reach similar functional endpoints while displaying different patterns of tissue and molecular injury. This distinction should be considered when treatment effects observed in chemotherapy-induced POI are interpreted in the broader context of ovarian aging.

Several limitations should be considered when interpreting these findings. First, natural reproductive aging and chemotherapy-induced POI were examined at single experimental endpoints. The present study therefore compares the ovarian states observed at these time points rather than the full temporal trajectories through which they develop. Second, transcriptomic profiling was performed using whole ovarian tissue. Changes in gene expression may consequently reflect both transcriptional regulation within individual cell populations and differences in ovarian cellular composition. Cell type-specific approaches will be useful for resolving the cellular sources of these signals in future studies. Finally, fertility represents an integrated reproductive outcome and can be influenced by age-related changes outside the ovary, particularly in naturally aged animals. These limitations do not affect the direct phenotypic comparison between the two models but should be considered when interpreting the molecular differences and their relationship to reproductive function.

Conclusion

Natural reproductive aging and chemotherapy-induced POI both led to loss of ovarian reserve, disrupted estrous cycles, endocrine dysfunction, and reduced fertility. However, the underlying patterns of ovarian injury were not identical. Naturally aged ovaries showed more prominent cellular senescence, extracellular matrix remodeling, and fibrosis, whereas chemotherapy-induced POI was associated with stronger DNA damage, oxidative stress, apoptosis, and inflammatory signaling. The transcriptomic findings were consistent with these differences and also identified molecular changes shared by the two models.

Chemotherapy-induced POI therefore reproduces several important features of natural ovarian aging but does not fully reflect the biological changes that accompany reproductive aging. This distinction is relevant when these models are used to study ovarian dysfunction or evaluate potential therapies. Improvements observed in chemotherapy-induced POI should be interpreted within the context of that injury model rather than assumed to represent the same response in naturally aged ovaries. Considering both the shared features and the differences between these conditions may allow more appropriate model selection and more accurate evaluation of strategies aimed at preserving ovarian function and fertility.

Declarations

Acknowledgments

The authors acknowledge the technical support provided by the participating institutions and research personnel involved in the experimental procedures and transcriptomic analyses.

Funding

This work was supported by the National Natural Science Foundation of China (grant no. 82501955); the Natural Science Foundation of Hebei Province (grant no. H2026206526);

Author contributions

Yuanmeng Zhang, Zhongkang Li, and Xianghua Huang conceived and designed the study. Yuanmeng Zhang, Ni Yang, and Shangxuan Song performed the animal experiments. Yuanmeng Zhang, Ni Yang, Shangxuan Song, Chunli Qin, Yingqian Wang, Yanyan Liu, Jiahua Zheng and Xiaotong Xu conducted the histological and molecular experiments. Yuanmeng Zhang, Yuanzheng Ning, and Jingkun Zhang performed the transcriptomic and statistical analyses. Yuanmeng Zhang, Ni Yang, Shangxuan Song, Zhongkang Li, and Xianghua Huang interpreted the results. Yuanmeng Zhang, Ni Yang, and Shangxuan Song prepared the figures. Yuanmeng Zhang drafted the manuscript. Zhongkang Li and Xianghua Huang supervised the study and critically revised the manuscript. All authors reviewed and approved the final manuscript.

Data availability statement

The raw RNA-sequencing data generated during the current study have been deposited in the National Center for Biotechnology Information Sequence Read Archive under BioProject accession number PRJNA1559283 and are available at https://www.ncbi.nlm.nih.gov/bioproject/PRJNA1559283. Additional data supporting the findings of this study are available from the corresponding author upon reasonable request.

Disclosures

Conflict of interest

The authors declare no conflicts of interest.

Human rights statements and informed consent

This study did not involve human participants. Therefore, informed consent was not required.

Consent for publication

Not applicable.

Animal studies

All institutional and national guidelines for the care and use of laboratory animals were followed.

Approval by Ethics Committee

All animal experimental procedures were approved by the Animal Ethics Committee of the Second Hospital of Hebei Medical University (approval no. 2026-AE407).

Clinical trial registry

Not applicable. This study did not involve a clinical trial.

References

1. Li Q, Geng X, Zheng W, Tang J, Xu B, Shi Q. Current understanding of ovarian aging. Sci China Life Sci. 2012;55(8):659–69.
2. Davis SR, Lambrinoudaki I, Lumsden M, Mishra GD, Pal L, Rees M, et al. Menopause Nat Rev Dis Primers. 2015;1:15004.
3. Nash Z, Davies M. Premature ovarian insufficiency. BMJ. 2024;384:e077469.
4. Touraine P, Chabbert-Buffet N, Plu-Bureau G, Duranteau L, Sinclair AH, Tucker EJ. Premature ovarian insufficiency. Nat Rev Dis Primers. 2024;10(1):63.
5. Isola JVV, Ocañas SR, Hubbart CR, Ko S, Mondal SA, Hense JD, et al. A single-cell atlas of the aging mouse ovary. Nat Aging. 2024;4(1):145–62.
6. Liu M, Qiu Y, Xue Z, Wu R, Li J, Niu X, et al. Small extracellular vesicles derived from embryonic stem cells restore ovarian function of premature ovarian failure through PI3K/AKT signaling pathway. Stem Cell Res Ther. 2020;11(1):3.
7. Lin Z, Li Y, Zhao Y, Liu D, Deng S, Gu J, et al. Antifibrotic drug finerenone restores fertility in premature ovarian insufficiency. Science. 2026;391(6785):eadz4075.
8. Dai F, Wang R, Deng Z, Yang D, Wang L, Wu M, et al. Comparison of the different animal modeling and therapy methods of premature ovarian failure in animal model. Stem Cell Res Ther. 2023;14(1):135.
9. Zhang T, Yan D, Yang Y, Ma A, Li L, Wang Z, et al. The comparison of animal models for premature ovarian failure established by several different source of inducers. Regul Toxicol Pharmacol. 2016;81:223–32.
10. Spears N, Lopes F, Stefansdottir A, Rossi V, De Felici M, Anderson RA, et al. Ovarian damage from chemotherapy and current approaches to its protection. Hum Reprod Update. 2019;25(6):673–93.
11. Zhao Y, Ma J, Yi P, Wu J, Zhao F, Tu W, et al. Human umbilical cord mesenchymal stem cells restore the ovarian metabolome and rescue premature ovarian insufficiency in mice. Stem Cell Res Ther. 2020;11(1):466.

12. Yang Y, Tang X, Yao T, Zhang Y, Zhong Y, Wu S, et al. Metformin protects ovarian granulosa cells in chemotherapy-induced premature ovarian failure mice through AMPK/PPAR-γ/SIRT1 pathway. Sci Rep. 2024;14(1):1447.
13. Zhou XY, Lai YH, Zhang J, Li Y, Wu XM, Yang YZ, et al. Advanced oxidation protein products attenuate the autophagy-lysosome pathway in ovarian granulosa cells by modulating the ROS-dependent mTOR-TFEB pathway. Cell Death Dis. 2024;15(2):161.
14. Xu X, Wang J, Jin X, Ma Q, Li H, Zhou Q, et al. Bu-Shen-Ning-Xin decoction ameliorates premature ovarian insufficiency by suppressing oxidative stress through rno_circRNA_012284/rno_miR-760-3p/HBEGF pathway. Phytomedicine. 2024;133:155920.
15. Zhao F, Yan L, Zhao X, Wu J, Fang Y, Xin Z, et al. Aberrantly high FBXO31 impairs oocyte quality in premature ovarian insufficiency. Aging Dis. 2024;15(2):804–23.
16. Chen Y, Zhang J, Tian Y, Xu X, Wang B, Huang Z, et al. Iron accumulation in ovarian microenvironment damages the local redox balance and oocyte quality in aging mice. Redox Biol. 2024;73:103195.
17. Umehara T, Winstanley YE, Andreas E, Morimoto A, Williams EJ, Smith KM, et al. Female reproductive life span is extended by targeted removal of fibrotic collagen from the mouse ovary. Sci Adv. 2022;8(24):eabn4564.
18. Jin M, Yu Y, Huang H. An update on primary ovarian insufficiency. Sci China Life Sci. 2012;55(8):677–86.
19. He S, Zhang X, Zhou W, Chen Y, Liu F, Wang W, et al. Retinoic acid and calcitriol protect mouse primordial follicles from cyclophosphamide treatment-induced apoptosis. Antioxid (Basel). 2026;15(1):68.
20. Wu M, Zhu Q, Xiong J, Tang W, Chen D, Xue L, et al. Modulating IL-11-dependent matrix stiffness to delay ovarian aging. Nat Aging. 2026;6(7):1395–416.
21. Briley SM, Jasti S, McCracken JM, Hornick JE, Fegley B, Pritchard MT, et al. Reproductive age-associated fibrosis in the stroma of the mammalian ovary. Reproduction. 2016;152(3):245–60.
22. Amargant F, Manuel SL, Tu Q, Parkes WS, Rivas F, Zhou LT, et al. Ovarian stiffness increases with age in the mammalian ovary and depends on collagen and hyaluronan matrices. Aging Cell. 2020;19(11):e13259.
23. Pei L, Wang W, Guo P, Qiao A, Duan X, Xu X, et al. Integrated analysis of differential m6A methylation and transcriptome profiles in ovaries of young and aged Qira black sheep. BMC Genomics. 2026;27:251.
24. Pietroforte S, Amargant F. Increased stiffness mimicking ovarian aging induces a fibroinflammatory response in follicles and impairs oocyte quality. Reproduction. 2026;171(2):xaaf026.
25. Yang Q, Chen W, Cong L, Wang M, Li H, Wang H, et al. NADase CD38 is a key determinant of ovarian aging. Nat Aging. 2024;4(1):110–28.

Figures

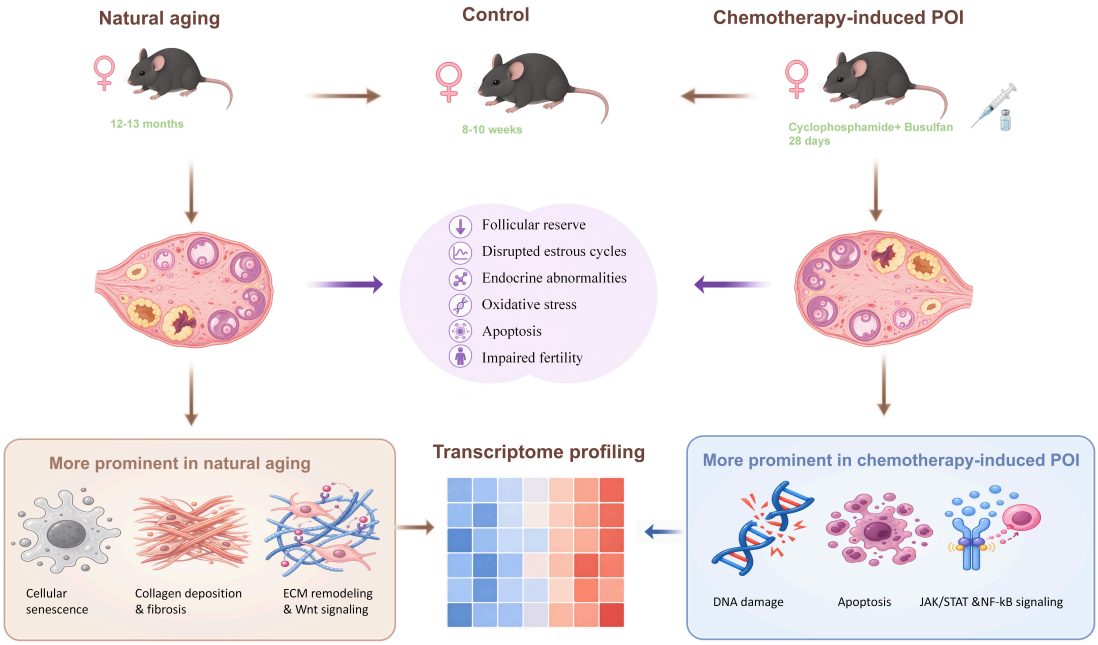


Figure 1

Ovarian functional and reproductive endocrine changes in naturally aged and chemotherapy-induced POI mice.

(A) Representative vaginal smears showing the four stages of the estrous cycle. **(B)** Representative estrous cycle profiles in the CON, NA, and POI groups. **(C)** Numbers of primary, secondary, antral, and atretic follicles. **(D)** Representative hematoxylin and eosin-stained ovarian sections. **(E)** Ovarian index. **(F)** Distribution of normal, prolonged, and irregular estrous cycles. **(G)** Changes in body weight during the observation period. **(H–J)** Serum concentrations of estradiol (E2), follicle-stimulating hormone (FSH), and luteinizing hormone (LH), respectively. CON, young control group; NA, natural aging group; POI, chemotherapy-induced premature ovarian insufficiency group. Data are presented as mean ± standard deviation (SD). Estrous cycles were evaluated in eight mice per group. Statistical comparisons were performed using one-way analysis of variance (ANOVA) followed by Tukey's multiple-comparison test, two-way repeated-measures ANOVA for body weight, and the chi-square test or Fisher's exact test for categorical variables, as appropriate. *P < 0.05, **P < 0.01, ***P < 0.001, and ****P < 0.0001; ns, not significant.

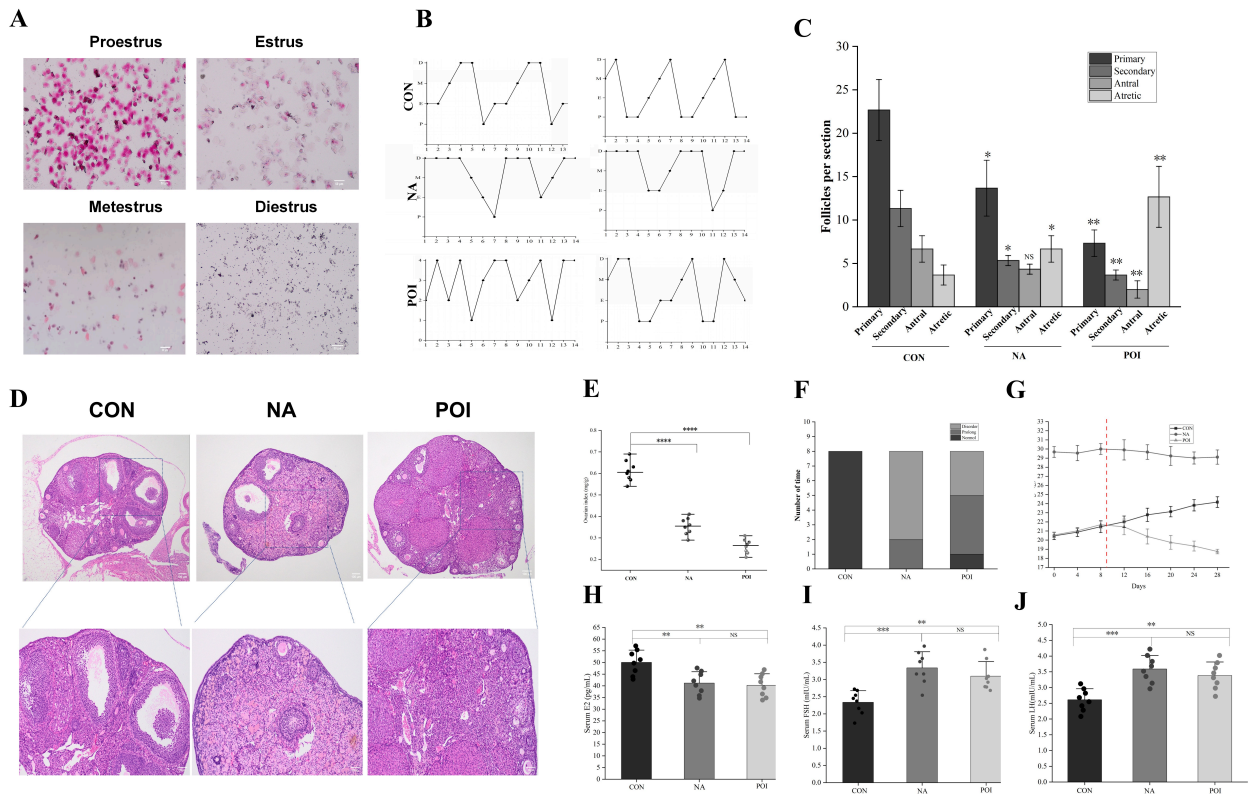


Figure 2

Ovarian apoptosis and senescence-associated changes in natural aging and chemotherapy-induced POI.

(A) Representative TUNEL staining of ovarian sections from the CON, NA, and POI groups. Green fluorescence indicates TUNEL-positive signals, and blue fluorescence indicates DAPI-stained nuclei. **(B)** Representative senescence-associated β-galactosidase (SA-β-gal) staining. **(C)**Quantification of TUNEL-positive cells. **(D)** Quantification of SA-β-gal-positive areas. **(E)** Western blot analysis of caspase-9, caspase-3, and Bcl-2 protein expression. **(F)** Densitometric quantification of protein expression normalized to β-actin. CON, young control group; NA, natural aging group; POI, chemotherapy-induced premature ovarian insufficiency group; TUNEL, terminal deoxynucleotidyl transferase-mediated dUTP nick-end labeling; DAPI, 4',6-diamidino-2-phenylindole. Data are presented as mean ± SD (n = 3 biological replicates per group). Statistical comparisons were performed using one-way ANOVA followed by Tukey's multiple-comparison test. **P < 0.01, ***P < 0.001, and ****P < 0.0001; ns, not significant..

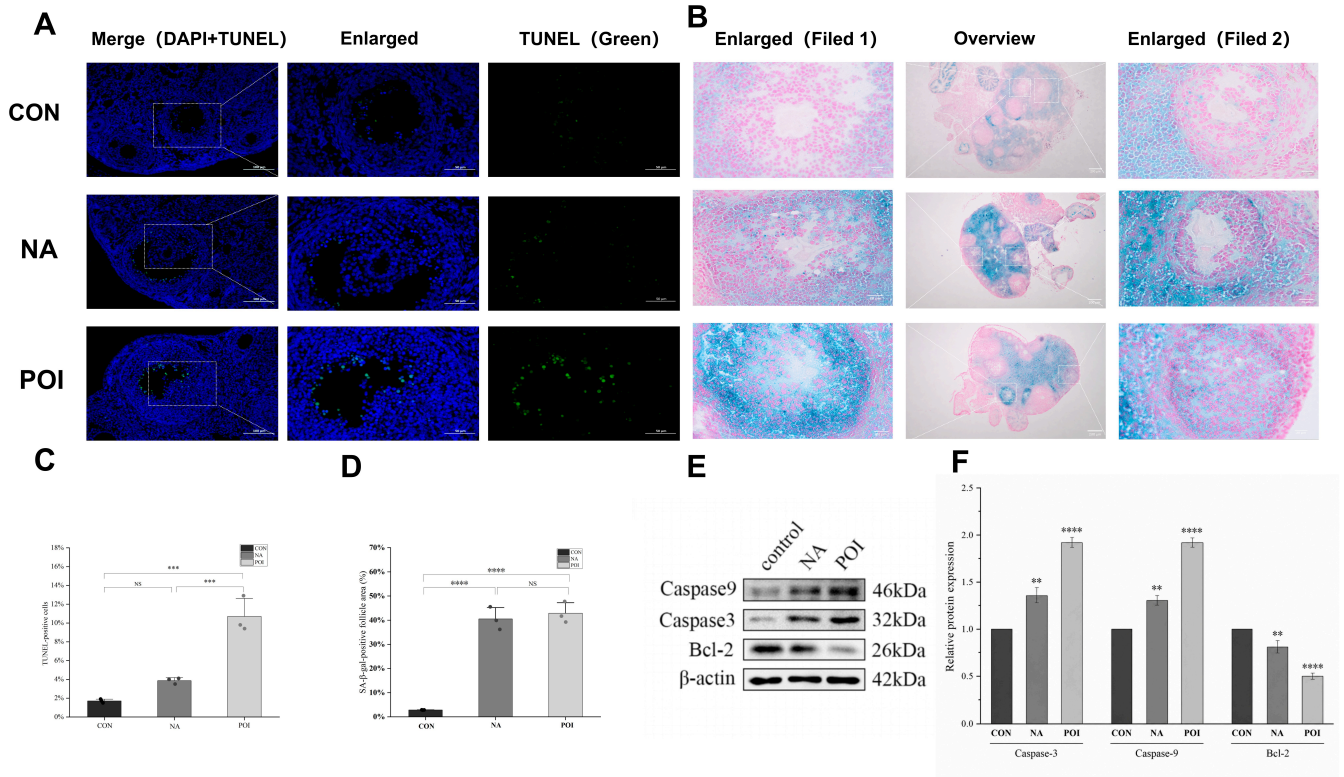


Figure 3

Ovarian senescence, DNA damage, collagen deposition, and oxidative stress in natural aging and chemotherapy-induced POI.

(A) Representative immunohistochemical staining for p21, p16, γH2AX, and collagen I in ovarian tissues from the CON, NA, and POI groups. **(B–E)**Quantification of p21-, p16-, γH2AX-, and collagen I-positive staining, respectively. **(F)** Ovarian malondialdehyde (MDA) levels. **(G)**Ovarian reactive oxygen species (ROS) levels. **(H)** Glutathione peroxidase (GSH-Px) activity. **(I)** Total superoxide dismutase (T-SOD) activity. CON, young control group; NA, natural aging group; POI, chemotherapy-induced premature ovarian insufficiency group; γH2AX, phosphorylated histone H2AX. Data are presented as mean ± SD (n = 3 biological replicates per group). Statistical comparisons were performed using one-way ANOVA followed by Tukey's multiple-comparison test. *P < 0.05, **P < 0.01, ***P < 0.001, and ****P < 0.0001; ns, not significant.

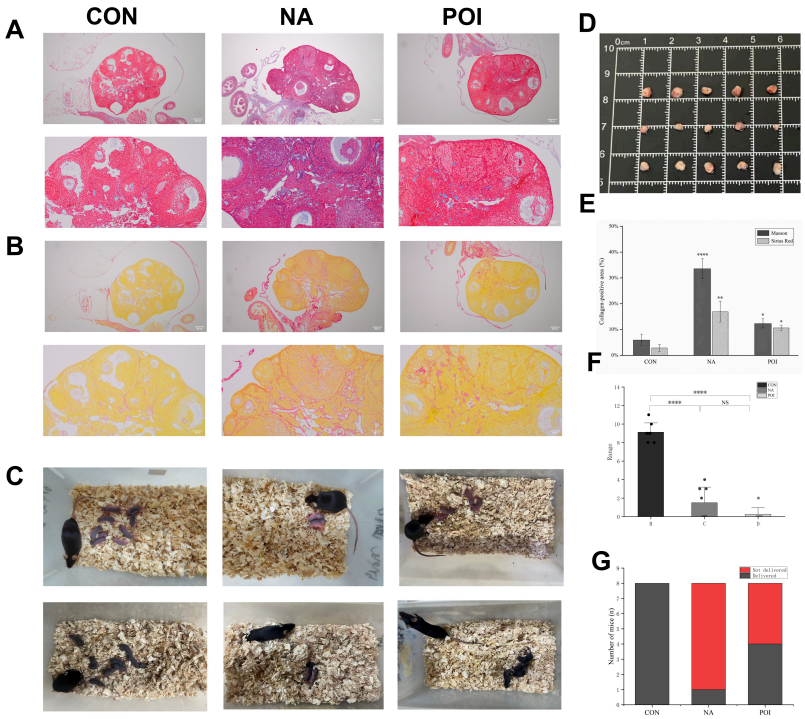


Figure 4

Ovarian fibrosis and reproductive capacity in natural aging and chemotherapy-induced POI.

(A) Representative Masson trichrome staining of ovarian sections. **(B)**Representative Sirius Red staining of ovarian sections. **(C)**Representative photographs illustrating reproductive outcomes following mating. **(D)** Gross ovarian morphology in the three experimental groups. **(E)**Quantification of collagen-positive areas detected by Masson trichrome and Sirius Red staining. **(F)** Number of live-born pups per female. **(G)**Numbers of females with and without successful delivery. CON, young control group; NA, natural aging group; POI, chemotherapy-induced premature ovarian insufficiency group. Data are presented as mean ± SD. Histological quantification was performed using three biological replicates per group, whereas fertility was assessed in eight females per group. Continuous variables were analyzed using one-way ANOVA followed by Tukey's multiple-comparison test. Delivery outcomes were evaluated using Fisher's exact test. *P < 0.05, **P < 0.01, ***P < 0.001, and ****P < 0.0001; ns, not significant.

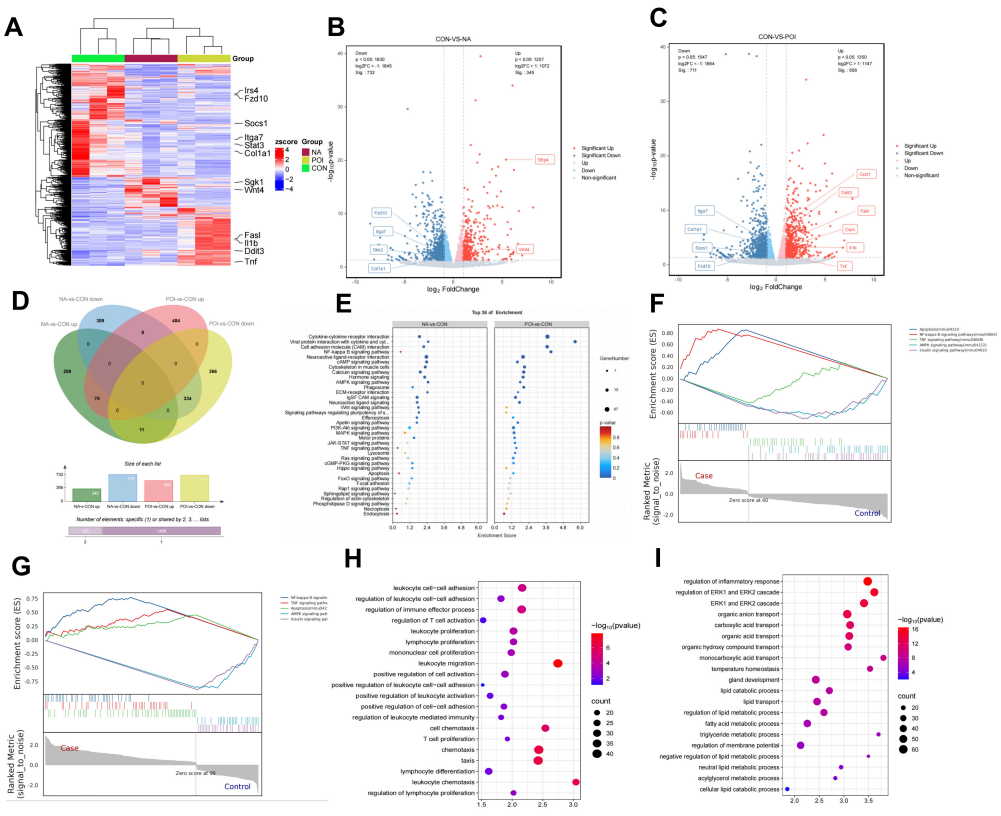


Figure 5

Transcriptomic profiling and functional enrichment analysis of ovaries from naturally aged and chemotherapy-induced POI mice.

(A) Hierarchical clustering heatmap of differentially expressed genes (DEGs) across the CON, NA, and POI groups. **(B, C)** Volcano plots showing DEGs in the NA versus CON and POI versus CON comparisons, respectively. **(D)**Overlap of upregulated and downregulated DEGs identified in the two comparisons. **(E)** Kyoto Encyclopedia of Genes and Genomes (KEGG) pathway enrichment analysis. **(F, G)** Gene set enrichment analysis (GSEA) of representative gene sets in the NA versus CON and POI versus CON comparisons, respectively. **(H)** Gene Ontology (GO) Biological Process enrichment analysis of DEGs in naturally aged ovaries, highlighting leukocyte adhesion, migration, activation, and related immune processes. **(I)** GO Biological Process enrichment analysis of DEGs in chemotherapy-induced POI ovaries, highlighting inflammatory responses, ERK1/ERK2 cascade regulation, and lipid metabolic processes. CON, young control group; NA, natural aging group; POI, chemotherapy-induced premature ovarian insufficiency group. Transcriptomic analysis was performed using three biological replicates per group.

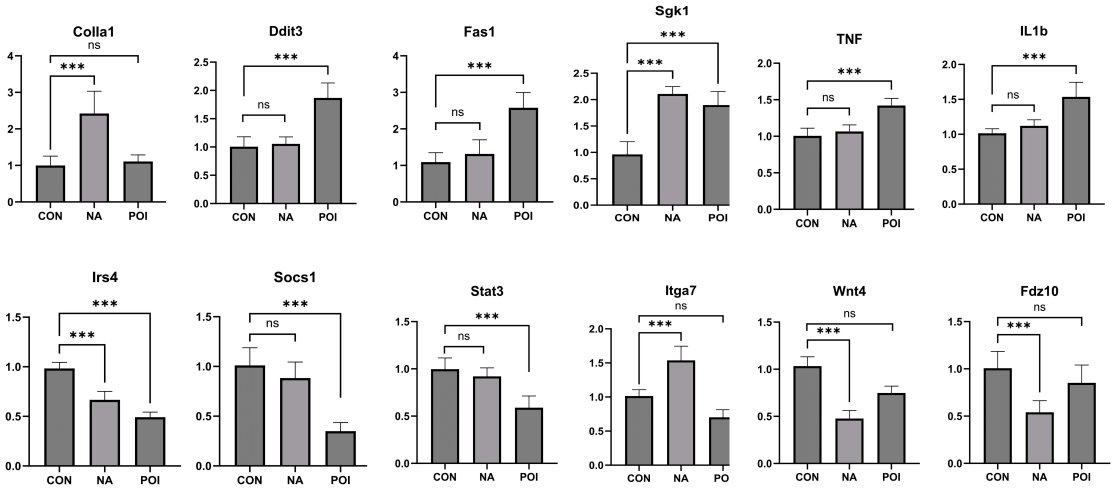


Figure 6

Quantitative real-time PCR validation of representative genes associated with ovarian aging and chemotherapy-induced POI.

Relative mRNA expression of Col1a1, Ddit3, Fasl, Sgk1, Tnf, Il1b, Irs4, Socs1, Stat3, Itga7, Wnt4, and Fzd10 was measured in ovarian tissues from the CON, NA, and POI groups. Col1a1 and Itga7 were selected as extracellular matrix-associated genes; Ddit3 and Fasl as cellular stress- and apoptosis-associated genes; Tnf and Il1b as inflammatory genes; Socs1 and Stat3 as JAK/STAT-related genes; Irs4 and Sgk1 as FoxO-related genes; and Wnt4 and Fzd10 as Wnt signaling-related genes. Expression levels were normalized to Gapdh. CON, young control group; NA, natural aging group; POI, chemotherapy-induced premature ovarian insufficiency group. Data are presented as mean ± SD (n = 3 biological replicates per group). Statistical comparisons were performed using one-way ANOVA followed by Tukey's multiple-comparison test. ***P < 0.001; ns, not significant.

Supplementary Files

This is a list of supplementary files associated with this preprint. Click to download.

- file.xlsx